International Journal for Multidisciplinary Research (IJFMR)
E-ISSN: 2582-2160 ● Website: www.ijfmr.com ● Email: editor@ijfmr.com

Biosynthesis of Antibacterial Walnut Shell Based Biochar and Corresponding Bi-Metallic Nanocomposite for Adsorption of Pharmaceutical Pollutant (Ciprofloxacin) From Water

Rakesh Kumar[1], Deepika Sharma[2], Anita Rani[3], Ajay Sharma[4], Ankita Sharma[5]

[1,2,4]Department of Chemistry, IEC School of Basic and Applied Science, Baddi, Solan, (174103) H.P. (India)
[3]Department of Chemistry, Baddi University of Emerging Science and Technology (BUEST), Baddi, Solan (173205) H.P. (India)
[5]Department of applied Sciences, University School of Computing, Rayat Bahra University, Mohali, (140104) Punjab, (India)

Abstract:
Environmental problems have grown as a result of the emergence of organic contaminants from industrial effluent. It is urgent to adopt and develop an efficient and sustainable technology for removing these pollutants before disposing of them in water resources due to the health risks they pose. In this sense, one of the most promising methods for cleaning up industrial pollution is adsorption employing metal oxides. To make these metal oxide more economical and safe, methods are adopted where the waste material from plant or plant based material are used to fabricate biochar (WBC) and then converted into metal encapsulated nanocomposite (Zn/Co-BC) using appropriate metal salts. This research includes the synthesis of walnut shell based biochar and then combination of Zinc and Cobalt to obtained respective nanocomposite. Both nanocomposites and biochar were accessed by variety of analytical instruments. Furthermore, batch adsorption process was conducted to remove Ciprofloxacin from the polluted water and adsorption was analysed by varying all the reaction conditions such as temperature, concentration, pH and agitation time etc. The (Zn/Co-BC) was also analysed to find the antibacterial activity against *Klebsiellia pneumonia* and *Staphylococcus aureus***.** The outcomes of both analyses declared biochar and metal encapsulated nanocomposite as tremendous adsorbent and antibacterial agent.

Keywords: Walnut shell; Biochar; Nanocomposite; Pollutant adsorption; Antibacterial agent.

Introduction:

Garbage management and water purification are difficult environmental problems. Due to its exceptional

qualities, such as cation exchange efficacy, carbon content, structural robustness ample and specific surface area biochar, a carbonaceous material made from a variety of organic waste (municipal sewage sludge, agricultural and household residues) has attracted a lot of attention **[1]**. Hazardous emissions such CO_2, NH_4 and SO_2 are released when waste is improperly disposed of in landfills **[2]**. Environmental and socioeconomic repercussions could result from a lack of understanding or information on sustainable waste management. Due to the fast growth of industrial activity, large amounts of heavy metals, including lead, zinc, manganese, copper, nickel and cadmium have been released, harming soil and water ecosystems **[3]**. These non-biodegradable and dangerous pollutants endanger human health even at very low concentrations because they contaminate the food chain and build up over time **[4-5]**. The thermal breakdown of biomass in an oxygen-free environment yields biochar, a carbon substance **[6-8]**. Layers of graphene and graphite structures and edge carbon atoms with functional groups like carboxylic, carbonyl and hydroxyl units make up this highly aromatic chemical **[9]**. Forest, sewage and agricultural wastes can be used to make an eco-friendly adsorbent **[10]**. Because the raw elements are plentiful and have little commercial value, biochar is a reasonably priced commodity. As the Biochar generated from waste organic products, they are thought to be effective and excellent pollutant adsorbent because of its financial advantages, favourable surface properties, broad raw material availability and low manufacturing costs **[11]**. Porous structure, high surface area and thermal stability are very less benefits that nanocomposite offer when act as adsorbent **[12-13]**. Shell waste accounts for 67.5% of seed weight in small-scale cashew enterprises. After pulp and oils are extracted, cashew nut shells (CNS), a byproduct of the industry, are burnt, which has detrimental effects on the environment. Similarly matamba fruit shell **[14]**, Apricot Seed Pulp **[15]**, almond shell **[16]**, pistachio shells **[17]**, peanut shell **[18],** hazelnut shell **[19]** are used as adsorbents to remove the pollutants from the waste water and also contributes to soil contamination and smoke emissions (air pollution) which highlights the significance of finding environmentally friendly disposal methods. It is a crucial choice for land safety as it can lessen water and soil pollution. In order to improve the removal effectiveness of the contaminants, dried fruit shell biochar was made and chemically activated with 1 M KOH. The biochar fabricated from various shells of dry fruits, can be used as biological agents to inhibit harmful diseases such as anticancer, biosensing and antimicrobials etc. **[20]**. This research articles include the synthesis of organic biochar from waste shells of walnut dry fruits and their encapsulation with Co and Zn. The generated biochar is used to remove the toxic pollutants like Ciprofloxacin from the water sample as well as antibacterial agent.

Material:

All the chemicals used in this research work were purchased from Sigma-Aldrich. All the used solvents were of analytical grade.

Instrumentation:

The availability of functional groups in synthesized Walnut recovered Biochar and corresponding nanocomposite i.e. (WBC) and (Zn/Co-BC) were initially identified by using FTIR, PerkinElmer® Spectrum™ 400 FT-IR/NIR spectrometer, to compare the characterstics features of both. Additionally, energy-dispersive X-ray spectroscopy (EDX, BRUKER,) was employed to analyze the elemental composition, purity, and distribution within the nanoparticles. The size and shape were then evaluated using a high-resolution transmission electron microscopy model (HR-TEM, JEM2100 plus, Jeol). The

specific surface area and poresize distribution of the nanoparticles were measured using BET (Quantachrome Autosorb-iQ-MP/XR), and crystallinity was assessed using X-ray diffraction (XRD) analysis (X'Pert Pro XRD models).By examining mass changes over time or temperature, TGA (RT-2400°C) enables the study of chemical reaction kinetics, such as evaporation, decomposition, and stability, while DSC (Thermo Scientific <<<b/>ArctiX<<!b/> DSC) provided information about thermal stability, homogeneity, and dispersion of the synthesised moieties. Scanning electron microscopy (SEM, Hitachi SU 8010 Series) was used to analyse particle boundaries and surface morphology.

Procedure:

Synthesis of Biochar (WBC):

The walnut was purchased from local market of dist. Panchkula. The shells of walnut were initially washed with double distilled water and dried in the sun light for 1-2 days and minced, crushed and grinded to biosorbent particles of homogenous size. The sample was kept at 600^0C for 2 hours in a muffle furnace with absence of oxygen and 50^0C rise in temperature after every 20 minutes. The obtained jet black organic biochar was kept for cooling overnight. The obtained dried product was treated with N/10 NaOH followed by washing with dilute HCl. After filtering, the material was cleaned with double-distilled water until a neutral product was produced. The material was dried under the sun light for 3 days and then further stirred with sulphuric acid with a ratio of 60:40 and filtered in a sintered glass funnel. The obtained residue was washed with double distilled water till all the washings found neutral and dried for whole day and then grind it till it homogenous powder obtained.

Synthesis of metal encapsulated Biochar (Co/Zn-BC):

0.1M Zinc chloride and 0.1 M Cobalt nitrate was dissolved in isopropyl alcohol with 10 gm of synthesized biochar (WBC). The metal nanocomposite was deposited on the supported biochar after the reduction of metal salt by the addition of 0.012 moles of $NaBH_4$ with the continuous stirring for 2.0 h. Entire mixture was agitated until the gas from the mixture evolved completely. The stirring stopped and the content was allowed to settle down. After filtering and washing with distilled water, the residue was allowed to dry in a desiccator for three to four days at room temperature.

Thermodynamic study:

The process underlying the adsorption of adsorbates from the aqueous phase was investigated using adsorption isotherms.

Adsorption isotherms: Adsorption isotherms typically show an adsorbent's performance and clarify the sorbate-sorbent interaction process. Adsorption isotherms represent the equilibrium connection between sorbent and sorbate. Isotherms are commonly used to describe the ratio of the quantity of adsorbate adsorbed onto the surface of adsorbent to the equilibrium concentration of adsorbate in aqueous medium. Many isotherms have been described for the analysis of sorption experiment data. In this work, experimental results were analysed using the Langmuir, Freundlich, and Tempkin isotherm models. **[21]**.

Freundlich model: Freundlich model state that adsorption ensued on heterogeneous texture due to the assortment of adsorption sites. The logarithmic equation for this model can be expressed as below **[22]**.

$$\ln q_e = \ln k_f + \frac{1}{n(lnCe)} \quad \text{.....(3)}$$

Where Ce (mg/L) is the adsorbate's equilibrium concentrations or amount in solution and qe (mg/g) is the adsorbate's quantity adsorbed per unit mass of adsorbent at equilibrium. The Freundlich constants (K_f) (L/g) and "n" represent the adsorption intensity and capacity respectively. The values of K_f and 1/n can be computed from slope and intercept of a plot $\ln q_e$ vs. $\ln C_e$.

Tempkin model: This model elucidates the indirect interaction between adsorbate and adsorbent as well as sorption energy **[23]**. Tempkin equation can be explained as follow:

$Q_e = B\ln(k_T) + B\ln(C_e)$.....(4)

where k_T and B represents the Tempkin coefficients and calculated from the plot of qe against ln C_e.

Langmuir model: Langmuir model describes the homogeneous sorption, where all sites have same adsorbate affinity. Linearized form of this model can be represented as follow **[24]**:

$\frac{Ce}{Cq} = \frac{1}{kLQm} + \frac{Ce}{Qm}$.....(5)

Here k_L (L/mg) is the Langmuir's constant and Qm (mg/g) is the adsorbent's maximal monolayer ability. The slope and intercept of a plot of Ce vs. Ce/qe can be used to forecast the values of Qm and kL., respectively. The dimensionless factor (R_L) has been used to examine the feasibility of adsorption process at different initial concentrations. R_L values were computed from following Equation

$R_L = \frac{1}{1+(kLC0)}$.....(6)

Here C_0 (mg/L) is initial concentrations of adsorbates

Kinetics study: Adsorption determine effectiveness of an adsorbent to adsorb and is a time based process, required to determining efficacy of an adsorbent and examine its application on pseudo-first-order and pseudo-second-order **[25].**

Pseudo-first-order model: This kinetic model is based on mass transfer of adsorbate molecule from aqueous phase to the sorption sites. This model is expressed as:

$\text{Log}(q_e\text{-}q_r) = \log q_e - \frac{k1}{2.303t}t$.....(7)

k_1 access the h^{-1} (rate constant) , qe and qt provide amount of adsorbate which adsorbed (mg/g) at time t (min). The value of rate constants (k_1) and qe were determined from slope and intercept of a linear plot of $\log(q_e\text{-}q_t)$ vs. t, respectively.

Pseudo-second-order model: The adsorption kinetic can be elucidated in term of pseudo-second order model and equation given below

$\frac{t}{qe} = \frac{1}{k2qe2} + (\frac{1}{qe})\ t$.....(8)

k_2 represent the constant for second-order (g mg^{-1} min^{-1}). The values of k_2 and q_e (mg/g) was calculated from a plot of t/q_e vs t.

Stability and Regeneration of adsorbent:

The reusability of generated adsorbents was investigated throughout the desorption experiment of different pollutants under acidic or basic eluting agents. Different contaminants have been treated with different desorbing agents. Using 0.05M and 0.01 mol/L NaOH solutions for ciprofloxacin were desorbable **[26]**. For the desorption experiment, pollutants-loaded adsorbent was placed in Erlenmeyer flasks containing 50 mL solutions of desorbing agents. The suspensions were centrifuged to extract the adsorbent following four hours of mechanical stirring at 220 rpm. After the desorption process, pollutant equilibrium concentrations were measured. The adsorbents were renewed and utilised in subsequent cycles after being washed with distilled water.

Antibacterial analysis:

The in vitro antibacterial activity of synthesised biochar nanocomposite (Zn/Co-BC) against two different pathogenic strains of bacteria was evaluated using the disc plate diffusion assay **[27]**. Dimethyl

sulphoxide was used to create the stock solutions (1000 µg/ml). The culture medium plates were prepared for bacterial growth under sterile conditions using nutrient agar and potato dextrose agar, respectively. To assess the impact of the chemical on bacterial and fungal growth, various concentrations, such as 100, 200, and 300 µg/ml, were put onto 5 mm sterilised discs of the filter paper or in a hole (well) and incubated initially for 24 h and finally for 72 hours at 30°C, respectively. Amoxicillin was used as standard antibiotic drug to compare the activity.

Sub Procedure:

The computational works for this research work was done by using OriginPro 8.5 software, where the data received for different analysis like XRD, TGA, DSC, XPS and BET etc. was transformed into graphical form.

Results and Discussion:

FTIR Analysis: The O-H stretching vibrations of hydroxyl groups were represented by a large absorption band at 3677 cm^{-1} in the FTIR spectra of walnut shell biochar (WBC), whereas aliphatic C-H stretching was identified by the peaks at 2973 and 2919 cm^{-1} **(Fig. 1, b)**. The absorption bands at 1700 and 1590 cm^{-1} originated from C=O stretching of carbonyl groups and aromatic C=C vibrations, respectively in the same spectrum **(Fig. 1, a)**. The peaks at 1439, 1205, and 1033 cm^{-1} were attributed to C-O and C-O-C stretching vibrations of oxygen-containing functional groups **[28]**. After Zn-Co loading, the O-H band shifted to 3326 cm^{-1} and the carbonyl vibration shifted from 1699 to 1652 cm^{-1} **[29]**, indicating coordination between Zn/Co species and surface hydroxyl/carboxyl groups indicting formation of bionanocomposites (Co/Zn-BC) **(Fig 1, b)**.

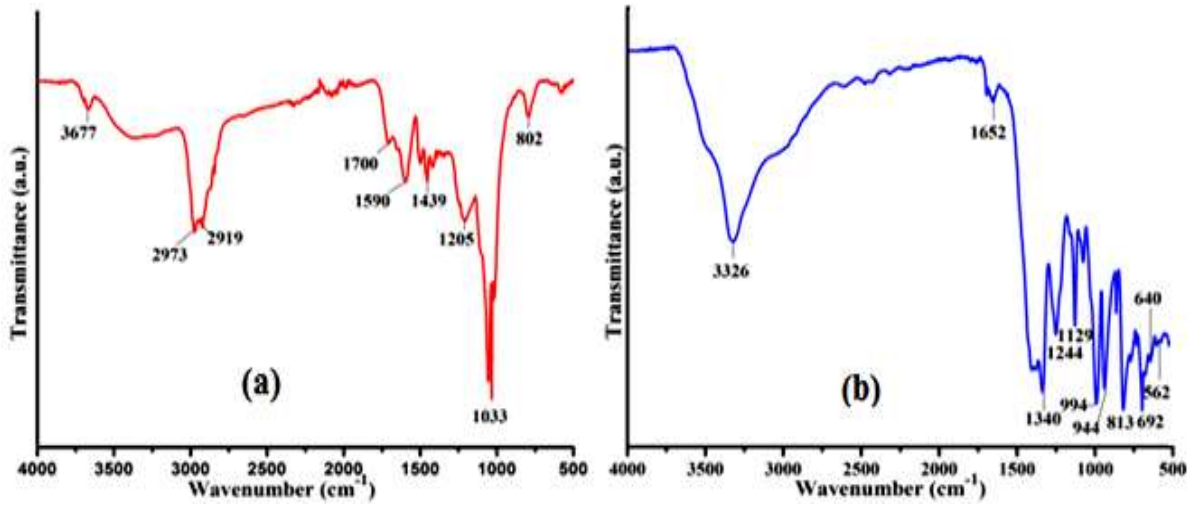

Fig. 1: FTIR Spectral evaluation of a) WBC and b) Zn/Co-BC

Furthermore, the appearance of new absorption bands at 692, 640 and 692 cm^{-1}, assigned to Zn-O and Co-O stretching vibrations, confirmed the successful immobilization of Zn-Co oxide nanoparticles onto the biochar matrix **[30]**. These spectrum alterations show that walnut shell biochar's oxygen-containing functional groups serve as metal species anchoring sites, resulting in the creation of a stable Zn-Co/biochar fabricated nanocomposite, or Co/Zn-BC.

XRD Analysis: The (002) plane of graphitic carbon is represented as a peak at 23.8º in the walnut shell nanocomposites XRD pattern **[31]**.

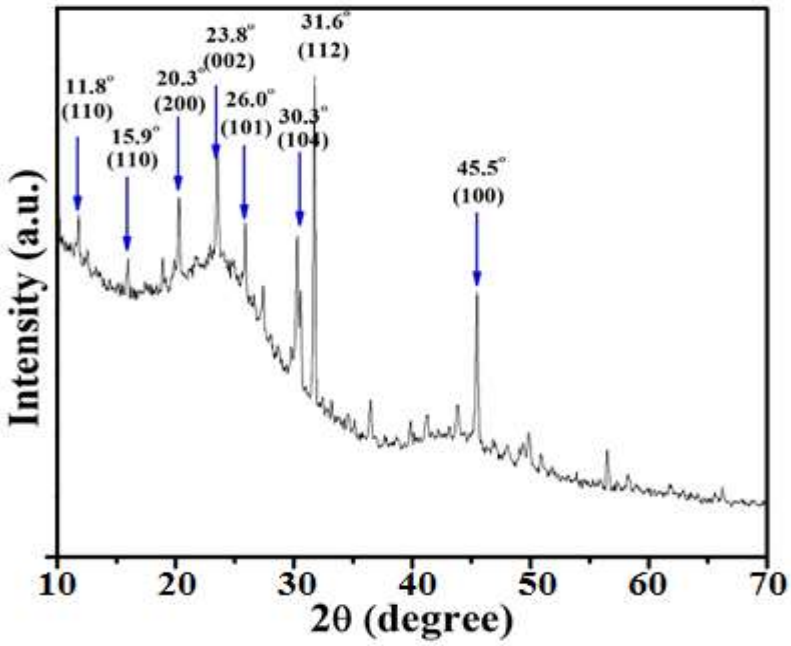

Fig. 2: XRD pattern exhibited by nanocomposite (Zn/Co-BC)

This peak indicates the presence of disordered carbon structure transformation into well organised nanocomposite material **(Fig. 2)**. A weak and broad around 45.5º is assigned to the (100) for crystalline-cobalt (Co) metal or mixed (Co-Zn) alloy **[32]**. On the other hand, besides of carbon peaks, several sharp peaks observed in the range of 11.8º, 15.9º and 20.3º correspond to crystalline cellulose, which arise from inorganic mineral residue naturally present in Zn/Co-BC. Peaks at 26.0º, and 30.3º are assigned to mineral ash components including silica, KCl, $CaCO_3$ containing compounds.

Peak at 31.6º (112) assign for Hexagonal wurtzite Zinc Oxide (ZnO) crystal **[33]**. The broad carbon peaks and sharp mineral peaks confirm that the walnut shell organic part is mainly amorphous while its metal encapsulated biochar showed crystalline inorganic phases.

XPS analysis: XPS elaborates the chemical bonding states, elemental composition and atomic concentrations available on the top 0 to 10 nanometres of the surface of the material **(Fig. 3)**. The most intense peak in the spectrum observed between 530 eV–531 eV corresponds to presence of oxygen in 1s orbital (O 1s) **[36]**. The main contribution was observed at 530 eV suggesting the lattice oxygen bond, might be for Co-O, and Zn-O bonding. A secondary peak observed at 531 eV confirm hydroxyl group **[37]**. The presence of another important peak (doublet) between 1021-1045 eV again confirming presence of (Zn $2p_{3/2}$) and also ΔE value of approximately 23 e V state the presence of Zn as Zn^{2+}.

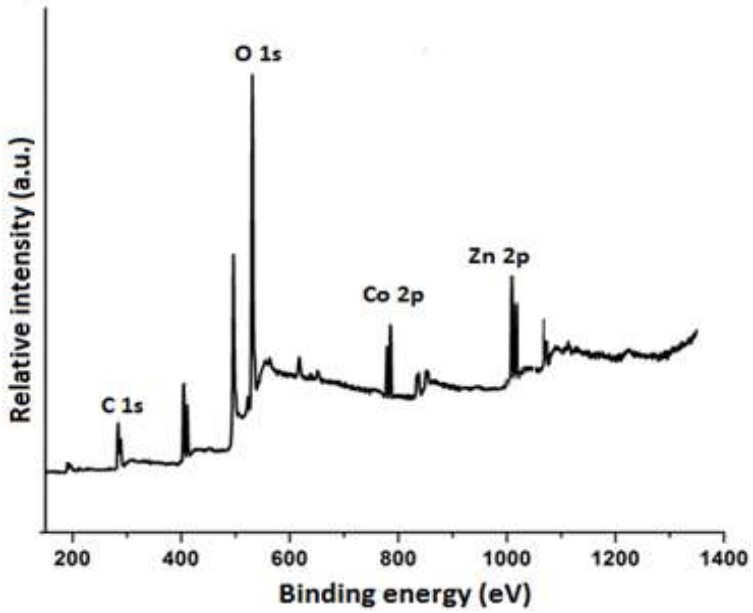

Fig. 3: XPS analysis of nanocomposite (Zn/Co-BC)

Similarly peak between (~780 eV–796 eV) confirm that the Co $2p_{3/2}$ and Co $2p_{1/2}$. C 1s at (~284.8 eV) peak is routinely used as the internal standard reference point to correct for surface charging effects across all electrical insulating sample. Hence, all the peaks appeared in the XPS spectra revealed the encapsulation of Zinc and Cobalt (Zn/Co) on the surface of fabricated biochar (WBC) proving the formation of metal encapsulated biochar (Zn/Co-BC).

FESEM: The micrographs capture two distinctly different materials or structural phases, evaluated at different spatial magnifications indicated by **(Fig. 4, a-d)**.

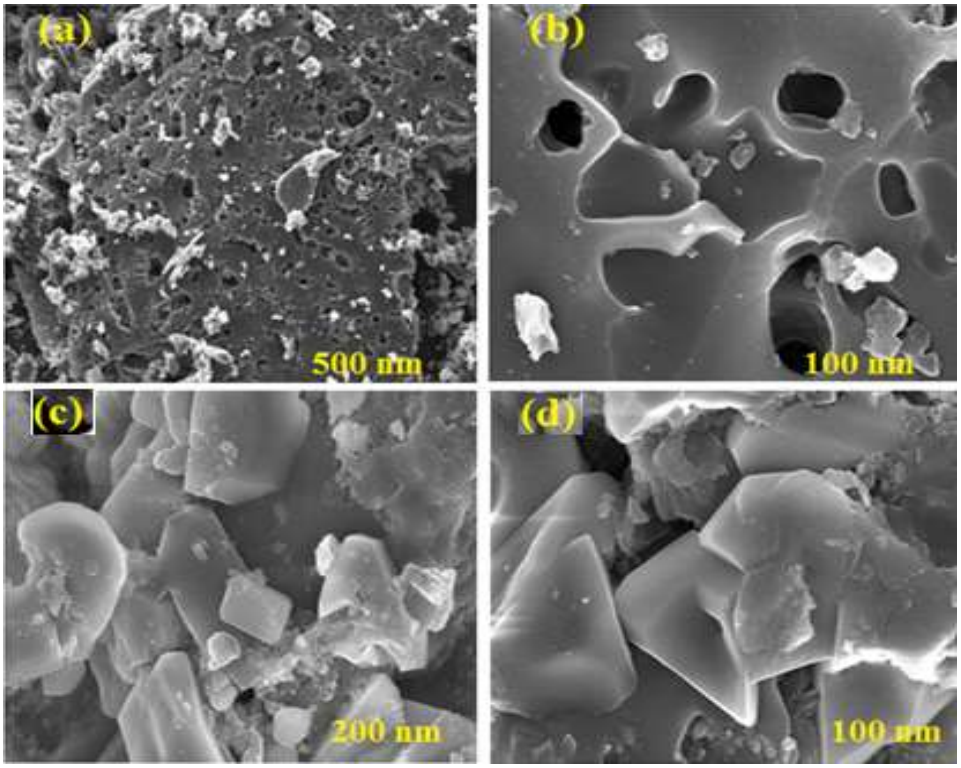

Fig. 4: FESEM images showing surface morphology of a) and b) WBC and c), d) Zn/Co-BC at different magnifications

Macroscopic overview of a highly rough, interconnected, and sponge-like porous matrix shown in **(Fig. 4, a)** corresponds to organic biochar where the material can be declared as highly porous **(Fig. 4, b)**. At 100 nm, high-magnification detailed view highlighting a smooth, glassy skeletal carbon structure containing rounded and elliptical intrapore surface **[38-39]**. **(Fig. 4, c)** at 200 nm magnification displays an ensemble of heavily agglomerated, angular solid particles featuring heterogeneous grain sizes while at 100 nm shows distinct, well-defined sharp facets and rigid crystalline structures resembling polyhedral nanocomposite. The major difference between **(Fig. 4 a,b)** with that of **(Fig. 4 c,d)** is that the high surface area biochar or carbon matrix with fast adsorption efficiency into a metal oxide crystalline solid or a modified biochar might showing better adsorption efficiency **[40]**.

HRTEM: FESEM image elaborate the size, crystal and morphology of the WBC and Zn/Co-WBC at different magnification **(Fig. 5)**. At 200 nm image **(Fig. 5, a)** showed a broad clustered or agglomerates showing a sheet like surface of WBC **[41]**. While **(Fig. 5, b)**, at 100 nm described the surface structure of Zn/Co-WBC showing agglomeration of Zn and Co in the core of organic biochar, confirming synthesis of required nanocomposites **[42]**.

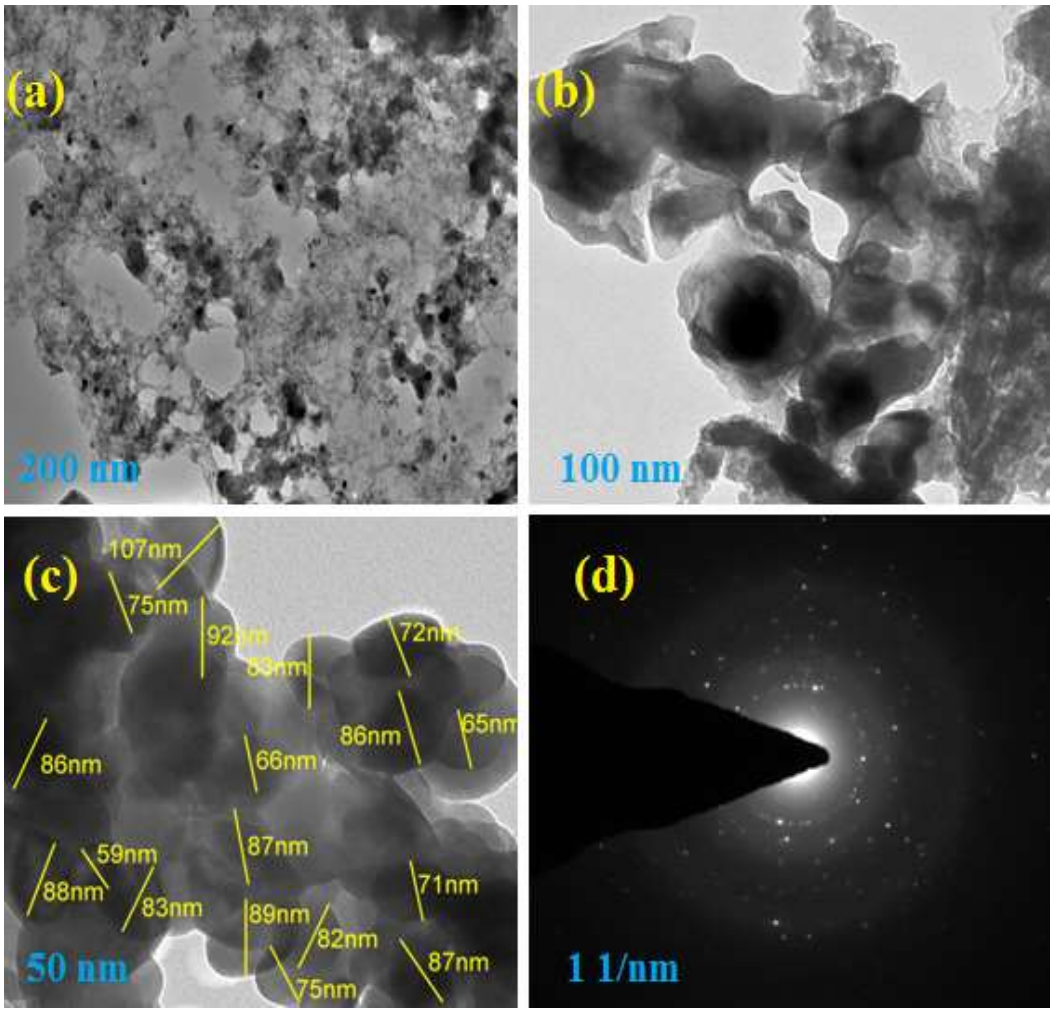

Fig. 5: HRTEM images of a) WBC, b) Zn/Co-BC showing internal morphology, c) Zn/Co-BC showing particle size and d) SAED pattern of Zn/Co-BC

The size of nanoparticles ranged from 58 nm to 107 nm identified from fig. c when it is zoomed at 50 nm, confirming nanostructured composite **(Fig. 5, c)**. SAED pattern describe the bright, arranged

concentric rings of individual spots indicating polycrystalline nature of Zn/Co-WBC which comprise many small crystalline grains **(Fig. 5, d)**.

BET analysis: As seen in **(Fig. 6)**, the Brunauer–Emmett–Teller (BET) graph elaborates the surface area and pore-related characteristics of the tested nanocomposite (Zn/Co-BC). The adsorption of the nitrogen gas molecules is seemed to form monolayer at 100-200 relative pressure, which get converted into multilayer adsorption as pressure rises upto 600 **[43]**. This confirm that the multilayer gas adsorption keep on increasing with increment in pressure. The above findings as well as results from BJH analysis conclude the mesoporous behaviour of the nanocomposite having surface area 37.438m²/g, pore volume 0.025cc/g and pore diameter 17.254 nm declaring its efficiency as an excellent adsorbent **[44]**.

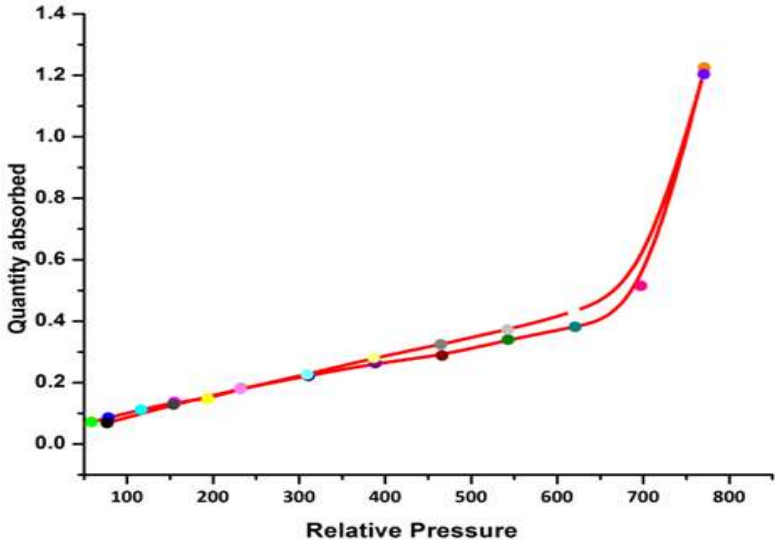

Fig. 6: Brunauer–Emmett–Teller graph shown by Zn/Co-BC in terms of

Adsorption and desorption of nitrogen gas

TGA/DSC: Using simultaneous TGA/DSC analysis, the thermal stability and phase transformation behaviour of Zn/Co-BC were assessed from room temperature to 900 °C **(Fig. 7)**. Between 91 °C and 246 °C, the TGA thermogram shows a single-stage, fast weight loss of almost 70% **(Fig. 7, a)**. The severe thermal event that occurred in the DSC curve **(Fig. 7, b)** at 96 °C, which is attributed to the loss of structural water, volatile components, or thermal breakdown of polymeric or organic frameworks, may be the cause of this striking weight loss **[45-46]**. Furthermore, no additional weight loss is seen above 246 °C, suggesting that the remaining 30% inorganic residue has exceptional thermal stability up to 900 °C. It's interesting to note that the DSC graph **(Fig. 7, b)** shows significant solid-state thermal changes in the high-temperature region where the uniform TGA baseline is observed, between 625 and 690 °C. In particular, two distinct, successive peaks are identified at 667 °C and 689 °C which pertain to intrinsic phase transitions, confirmed by the lack of weight changes in this regime **[47]**.

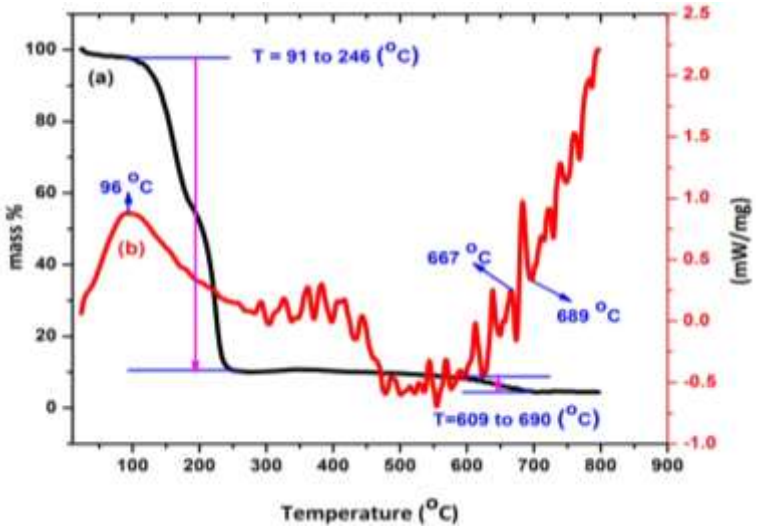

Fig. 7: a) TGA and b) DSC graph shown by Zn/Co-BC

These signals most likely represent successive crystalline lattice variations or a clearly defined melting-crystallization sequence of the thermally stable inorganic matrix.

Optimization of the experimental conditions:

Various parameters' effects on the adsorption % shown in **(Fig. 8),** describe their effect on all over adsorption process.

Influence of pH: As seen in **(Fig. 8, a)**, using WBC and Zn/Co-BC in a pH range of 2 to 7 (that is, pH 2.0, 2.5, 3.0, 3.5, 4.0, 4.5, 5.0, 5.5, 6.0, 6.5, 7.0, and 7.5) under optimal temperature (30°C), time of agitation i.e. (90 minutes), adsorbent amount of WBC and Zn/Co-BC (0.2 g), and starting Ciprofloxacin concentration (30 mg/L). The graph makes it evident that employing WBC and Zn/Co-BC nanocomposite, the adsorption of ciprofloxacin rises from 25 % to 78 % and 45% to 92% respectively **[48]**. The maximum adsorption in both cases was found at pH 5.5, which keeps on decreasing as the pH increases. Ciprofloxacin is generally present in three different ion forms: anionic, cationic and Zwitter ion. The cationic form is more common when the solution's pH is lower than pKa1. When an amino group is protonated, it exhibits an electrostatic attraction to the adsorbent surface. The surfaces of WBC and Zn/Co-BC are negatively charged at pH 5.5. Electrostatic attraction occurs between the cationic forms of the aqueous solution of ciprofloxacin **[49-50]**. Adsorption capability, however, drastically decreased when solution pH > pKa2. This might be the result of competition between hydroxyl ions and the anionic form of ciprofloxacin ions in an aqueous solution, or it could be the result of repulsion between negatively charged nanocomposite surfaces.

Influence of agitation time: The kinetic removal of CP ions has been studied under optimum initial concentrations about 30 mg/L as well as an adsorbent's dosage of 0.2 g with contact times varying from 30 to 180 minutes. Figure 8 illustrates the adsorption-absorption of ciprofloxacin from aqueous phase as a function of time **(Fig. 8, b)**. It was clear that the adsorption effectiveness of WBC and Zn/Co-BC increased significantly from 45% to 78% and 75% to 94%, respectively, when the agitation period was between 30 and 90 minutes **[51]**. The rapid uptake of Ciprofloxacin ions during the initial phases was primarily responsible for the larger striking possibility and abundantly available porous sites on the external surface of the adsorbents, which were quickly occupied by the action of Ciprofloxacin ions.

After 90 minutes, the adsorption percentage was decline might be due to occupancy of active sites on biochar and nanocomposite surface by Ciprofloxacin **[52]**.

Influence of adsorbent concentration: At the ideal concentration of ciprofloxacin (30 mg/L), the impact of adsorbent's dose was examined by changing its concentration from 30 mg/L to 240 mg/L. The effect of sorbent dosage on adsorption capacity is shown in **(Fig. 8, c)**. Ciprofloxacin removal efficiency improved from 35% to 70% for WBC and from 50% to 94% for Zn/Co-BC as the adsorbent dosage increased from 30 mg/L to 180 mg/L **[53-54]**. A more active areas and larger surface that are reachable at greater dosages are the reasons for this improvement. It could be due to the WBC and Zn/Co-BC nanostructure's higher specific surface area with many functional groups and increased availability of adsorbent sites. This makes it easier for the Ciprofloxacin ions to enter the WBC and Zn/Co-BC surface quickly. Nevertheless, no appreciable absorption occurred following the increment in loading dosage above 180 mg/L of both biochar and nanocomposite. It was explained by the fact that when the adsorbent molecules combine together, a cluster or aggregation of adsorbent particles forms **[55]**.

Influence of initial Ciprofloxacin concentration: The range of 30–180 mg/L was used to examine the impact of initial Ciprofloxacin concentration. The graph **(Fig. 8, d)** makes it evident that when the concentration of Ciprofloxacin increased from 30 mg/L to 180 mg/L, the percentage of adsorption dropped. Using WBC and Zn/Co-BC, the highest removal efficiency was determined to be 65% and 86%, respectively **[56]**. So, nanocomposite found to show the maximum adsorption efficiency compared to biochar alone. It was explained by the apparent large number of vacant active adsorption sites on the WBC and Zn/Co-BC surface at lower concentrations. The binding of Ciprofloxacin ions with the adsorbent molecules depends on these active sites. However, there were insufficient active sites at higher concentrations. Put differently, all Ciprofloxacin ions were engaging with the binding sites on the WBC and Zn/Co-BC surface at lower concentrations **[57]**.

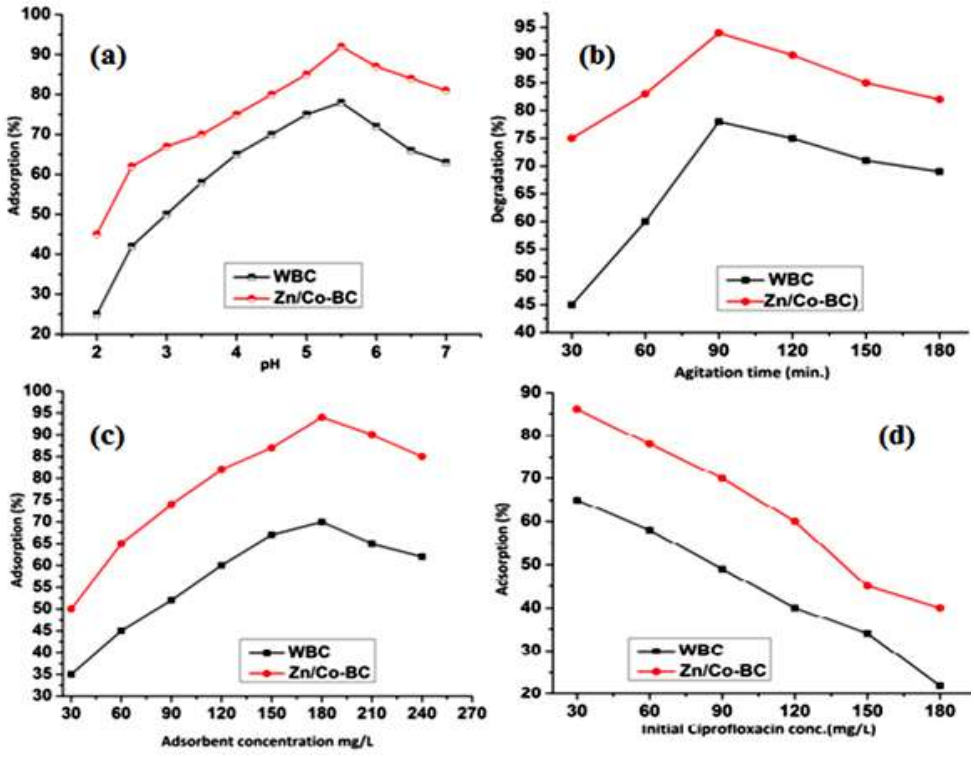

Figure 8: Influence of (a) pH (b) agitation time (c) adsorbent concentration and (d) initial Ciprofloxacin concentration on adsorption

This allows for more Ciprofloxacin ions to be adsorbed from the aqueous phase. In order to interact with the binding sites, the drug ions may compete with one another at increasing concentrations. Consequently, the adsorption absorption of Ciprofloxacin ions is decreased when all binding sites become saturated.

Influence of temperature: Ciprofloxacin elimination with WBC and Zn/Co-BC has been investigated at temperatures between 20 and 55 degrees Celsius as shown in **(Fig. 9)**. It has been discovered that the percentage of ciprofloxacin removed increases with temperature upto 45 degrees both in biochar and nanocomposite with maximum adsorption efficiency of 82% for WBC and 96% for Zn/Co-BC. This demonstrated a positive interaction between temperature and the adsorption mechanism that is congruent with its endothermic origin **[58]**. The main cause of the increased adsorption uptake was higher temperatures, which enhanced ciprofloxacin's binding affinity with the adsorbent's active site molecules. Furthermore, the activation energy provided at a higher temperature increased the pore structure and facilitated the flow of ciprofloxacin ions from aqueous systems, allowing it to more easily enter the adsorbent surface **[59]**.

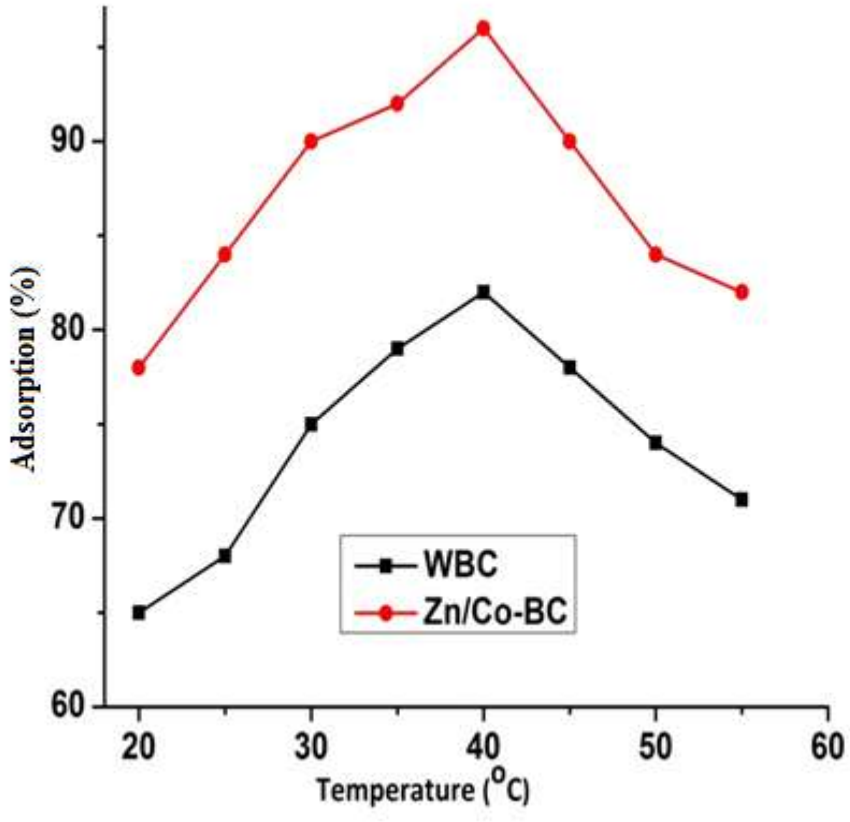

Fig. 9: Influence of temperature on adsorption of Ciprofloxacin pollutant

Thermodynamic studies: Adsorption isotherms, which also demonstrate the effectiveness of an adsorbent, are commonly used to clarify the sorbent-sorbate interaction mechanism. The equilibrium relationship between the sorbate and sorbent molecules is described by adsorption isotherms. In order to evaluate the sorption experimental data, numerous isotherms have already been established in the literature. The Langmuir, Freundlich, and Tempkin models were employed in our current investigation **(Fig. 10)**.

At low starting concentrations i.e. (C_e < 30 mg/L), $q_{(e)}$ grows dramatically. This implies that the adsorbate has a strong attraction for the active regions, which are initially abundant and unoccupied. The curves start to flatten out at greater concentrations; this plateau indicates that additional concentration increases do not considerably boost adsorption capacity because the active sites are becoming saturated.

Adsorption occurs via a monolayer mechanism on an energetically homogenous surface, according to the experimental findings, which closely matches the Langmuir model **[60]**. A finite number of uniform active sites are confirmed by the model's maximal monolayer capacity, which closely matches the experimental data.

The graphic suggested that the Langmuir model had a higher regression coefficient (R^2) value i.e. 0.94 and 0.99 for WBC and Zn/Co-BC respectively **(Fig. 10, b,a)**. The maximal capacity to adsorb (Qm) for ciprofloxacin, WBC, and Zn/Co-BC was also calculated using the Langmuir isotherm; the values of Qm were found to be 82.24 mg/g and 98.84 mg/g, respectively **(Table 1)**. However, the RL value was found to be between 0.514-0.147 and 0.254-0.0025 for biochar and nanocomposite respectively. Because R_L values fall between 0 and 1 for both WBC and Zn/Co-BC, the adsorption process was therefore possible **[61]**. Ciprofloxacin removal has been achieved with favourable and monolayer sorption onto WBC and Zn/Co-BC, according to the superior fit of the Langmuir isotherm. Consequently, adsorption behaviour can be approximated using the model of Langmuir isotherm

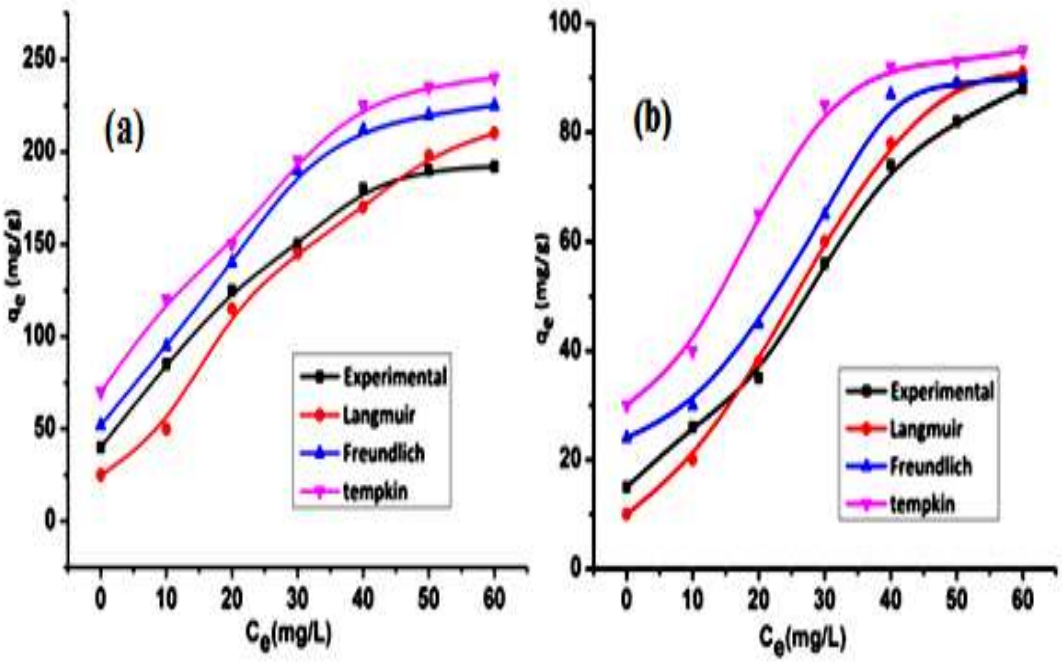

Fig. 10: Thermodynamic analysis exhibited by a) Zn/Co-BC and b) WBC

The Freundlich intensity parameter's value higher than one indicates a very advantageous adsorption process under all investigated conditions. The clear plateau at higher equilibrium concentrations, however, points to a departure from simply heterogeneous multilayer behaviour. The Temkin isotherm model assesses how important molecular interactions are to the adsorption process **[62]**. The linear reduction in the adsorption's heat suggests that the adsorbate-surface functionality interactions between groups have a moderate impact on the overall uptake capacity.

Table 1: Isotherm parameters for Ciprofloxacin removal by WBC and Zn/Co-BC

Sr. No	Adsorbents	WBC	Zn/Co-BC
	Parameters	**Ciprofloxacin (Adsorbate)**	**Ciprofloxacin (Adsorbate)**
a.	**Langmuir Isotherm**		
1.	Q_m (mg/g)	82.24	98.84
2.	K_L (L/mg)	0.538	0.914
3.	R_L	0.514-0.147	0.254-0.025
4.	R^2	0.94	0.99
b.	**Freundlich Isotherm**		
1.	K_F (L/g)	22.62	34.25
2.	n	5.74	8.95
3.	R^2	0.91	0.96
c.	**Tempkin Isotherm**		
1.	K_T (mg/g/h^2)	12.56	16.84
2.	B (g/mg/ h^2)	8.52	26.14
3.	R^2	0.97	0.98

Kinetic Study: A thorough investigation was conducted into the kinetic parameters for the adsorption of ciprofloxacin from the aqueous phase. The pseudo-first-order **(Fig. 11, a)**, pseudo-second-order **(Fig. 11, b)**, and Elovich **(Fig. 11, c)** and diffusion models **(Fig. 11, d)** were used to analyse the kinetic experimental data **[63]**. The applicability of the kinetics model was evaluated using a variety of fitting plots **(Fig. 11)**.

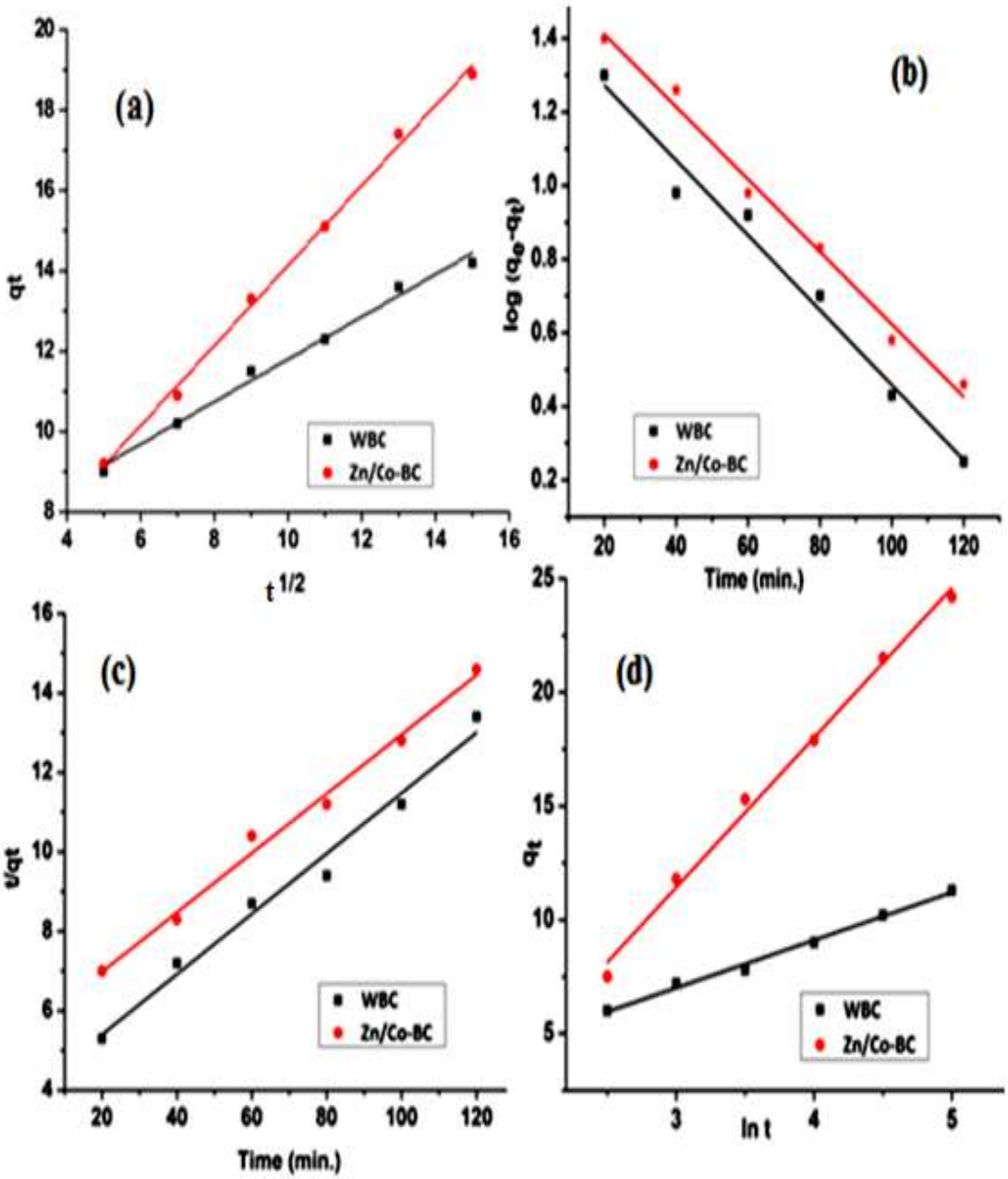

Fig. 11: Parameter analysis of Adsorption's Kinetic model showing (a) pseudo-1st order model, (b) pseudo-2nd order model (c) Elovich model and (d) diffusion model for WBC and Zn/Co-BC

(Table 2) shows that a pseudo-first-order with higher regression coefficient values i.e. 0.97 and 0.98, while pseudo-second-order with regression coefficient values 0.97 and 0.98 for WBC and Zn/Co-BC respectively, sufficiently explained the kinetics of Ciprofloxacin adsorption onto biochar and respective nanocomposite **[64]**. The As a result, the chemical mechanism mostly governed the adsorption process. Similar regression coefficient values of Elovich model and Diffusion model around 0.99 for both moieties were obtained showing excellent adsorption capacity **[65]**. The straight line graphs explain the occurrence of adsorption through chemisorption process.

Table 2: Adsorption Kinetic model parameters of (a) pseudo-1st order model, (b) pseudo-2nd order model (c) Elovich model and (d) diffusion model for WBC and Zn/Co-BC

Sr. No.	Adsorbents	WBC	Zn/Co-BC
	Parameters	Ciprofloxacin **(Adsorbate)**	Ciprofloxacin **(Adsorbate)**
a.	**Pseudo-1st order**		
1.	q_e (mg/g)	4.895	7.052
2.	K_1 (1/h)	0.038	0.054
3.	R^2	0.97	0.98
b.	**Pseudo-2nd order**		
1.	q_e (mg/g)	1.475	1.607
2.	K_2 (g/mg/min)	0.038	0.054
3.	R^2	0.97	0.98
c.	**Elovich model**		
1.	α(mg/g/h^2)	6.719	8.319
2.	B (g/mg)	2.097	6.582
3.	R^2	0.99	0.99
d.	**Diffusion model**		
1.	C (mg/g)	4.161	6.51
2.	K_{id}(mg g^{-1} $h^{1/2}$	0.528	0.997
3.	R^2	0.98	0.99

Thermodynamic parameter evaluation: Gibbs free energy (ΔG), entropy (ΔS), and enthalpy (ΔH) were used to assess the system's thermodynamic behaviour. These variables were routinely examined to see whether the adsorption process is feasible, whether it is exothermic or endothermic and how random or disordered the system is. In this study, the temperature was adjusted from 300-350 K while the concentration of Ciprofloxacin was kept at 20 mg/L **[66-67]**. All other parameters, including pH and adsorbent concentration etc. were held constant. Values of Gibbs free energy, Enthalpy and Entropy are given in **(Table 3)**.

Table 3: Thermodynamic values assessment of Ciprofloxacin adsorption for WBC and Zn/Co-BC

Sr. No.	Temperature (K)	ΔG° (KJ/mol)	
		WBC	**Zn/Co-BC**
1.	300	-4.45	-5.28
2.	310	-4.62	-5.52
3.	320	-4.72	-5.75

4.	330	-4.85	-5.82
5.	340	-4.98	-6.12
6.	350	-5.12	-6.48
7.	ΔH^o (KJ mol^{-1})	-11.49	-24.32
8.	ΔS^o (KJ mol^{-1})	-374.35	-384.54

(Table 3) provides an overview of ciprofloxacin's thermodynamic characteristics. As the Gibbs free energy change (ΔG°) was negative (-ve) at all examined temperatures and continued to rise with temperature, the adsorption process for WBC and Zn/Co-BC is both thermodynamically viable and spontaneous (Fig. 12). In both situations, the adsorption is exothermic because the enthalpy change (ΔH°) is negative [68–69].

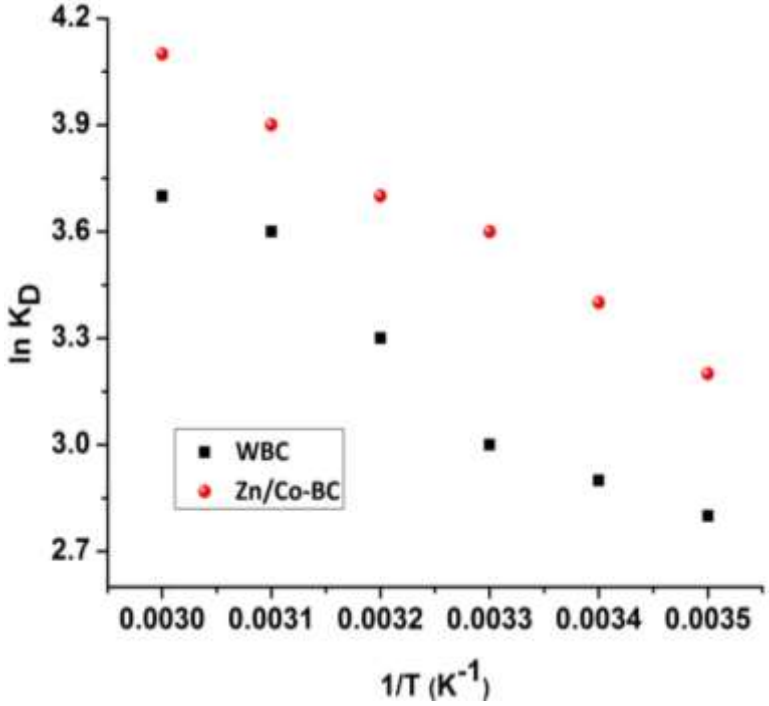

Figure 12: Thermodynamic parameter investigation of Ciprofloxacin's adsorption due to WBC and Zn/Co-BC

Furthermore, after Ciprofloxacin's adsorption upon the WBC and Zn/Co-BC surface, the negative entropy change (ΔS°) values (J/mol/K) demonstrate a reduction in the amount of randomness at the solid–liquid interface **[70]**.

Regeneration study: The WBC and Zn/Co-BC nanocomposite have undergone recyclability testing **[71]**. An optimal concentration was used for the experiment. Ciprofloxacin was first desorbed using a 0.01 mol/L NaOH solution as the desorbing agent in Erlenmeyer flasks. After being shaken for four hours at 220 rpm on a mechanical shaker, the suspension was centrifuged to produce WBC and Zn/Co-BC nanocomposite **[72]**. These were used for six cycles of reusability after being cleaned with ethanol and distilled water **(Fig. 13)**.

In this study, NaOH was used as the eluting agent to replenish the depleted adsorbents. 50 mg/L Ciprofloxacin solution was embedded on WBC and Zn/Co-BC for predefined contact duration before to

the regeneration process. 0.1 M NaOH may be able to desorb the colour molecules after saturation. Desorption is facilitated by the alkalinity of NaOH, which breaks the hydrogen-bonding and electrostatic contacts between the WBC's and Zn/Co-BC's surface functional groups and ciprofloxacin. **[73]**. The adsorbents were cleansed and oven-dried for 120 minute at 150 °C after desorption prior to reuse.

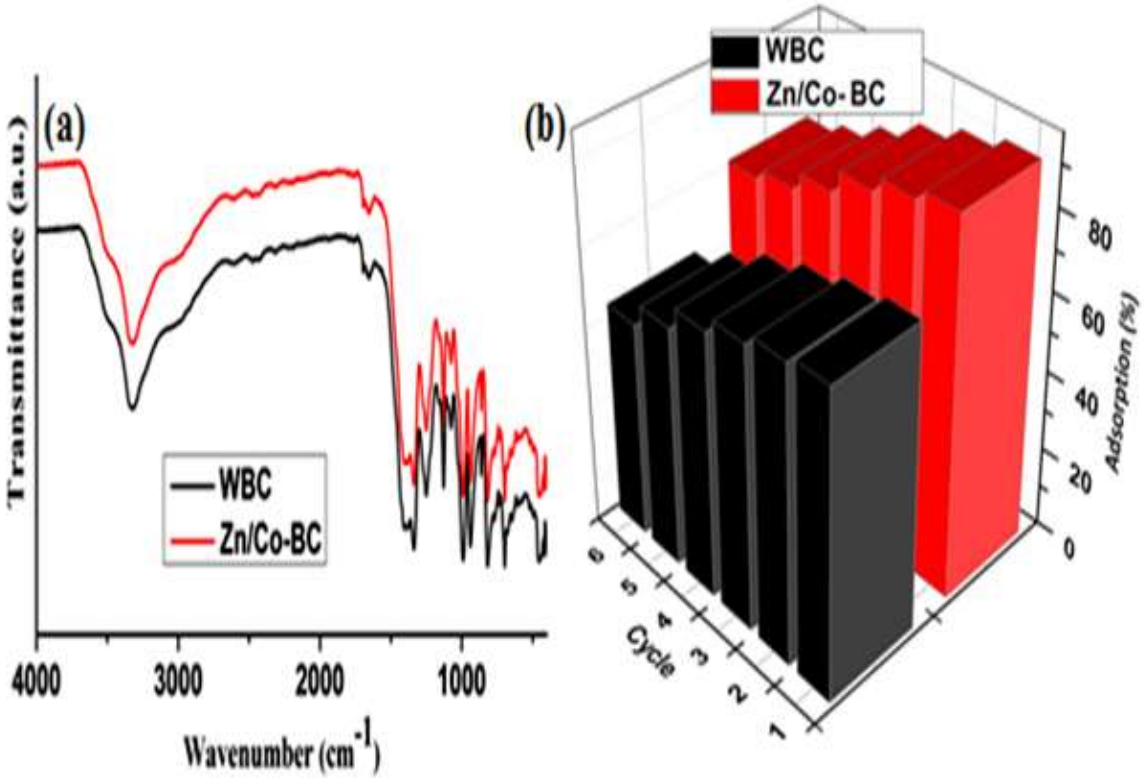

Fig. 13: Regeneration analysis of WBC and Zn/Co-BC adsorbents

WBC and Zn/Co-BC had regeneration efficiencies ranging from 75% to 54% and 93% to 72%, respectively. For up to six cycles, Zn/Co-BC and WBC were both successfully regenerated. The regeneration performance is shown in **(Fig. 13, b)**, which shows that Zn/Co-BC consistently performed better than WBC across all cycles **[74]**. The loss of functional groups upon repeated regeneration and physical and chemical alterations to the adsorbent surface are probably the causes of the consistent decline in efficiency **[75]**. FTIR spectra before and after adsorption has been studied to see the effect of adsorption on the quality of the nanocomposite and not any recognizable change in the composition were observed **(Fig. 13, a)**.

Antibacterial analysis: A variety of medicinal applications have made use of Zn and Co nanocomposites' well-known inhibitory qualities, most notably the inhibition of gram-positive and gram-negative bacterial strains **[76]**. The antibacterial efficacy of Zn/Co-BC generated in current work was subsequently assessed against both gram-positive and gram-negative bacteria, such as *Staphyllococus aureus* and *Klebsiellia pneumonia*.

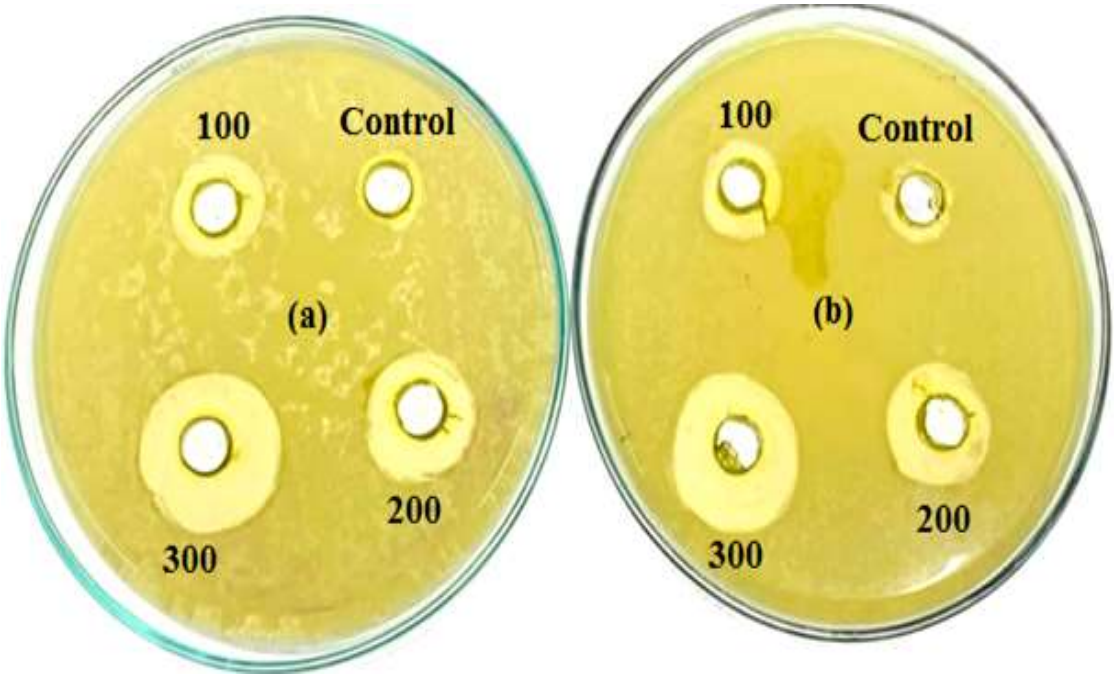

Fig. 14: Antibacterial activity shown by Zn/Co-BC against a) *Klebsiellia pneumonia* and b) *Staphyllococus aureus* at different concentrations (µg/ml)

It is believed that the impregnated nanocomposites' bactericidal activity involves their engagement with proteins of the cell, which results in inactivation, and their interaction with bacterial DNA, which condenses and stops DNA replication, resulting in apoptosis **[77]**.

Table 4: Antibacterial activity shown by Zn/Co-BC at different concentrations in terms of Zone of inhibition (mm)

		Zone of Inhibition	
	Concentration	***Klebsiellia pneumonia***	***Staphyllococus***
Zn/Co-BC	**100 µg/ml**	9 mm	10 mm
	200 µg/ml	13 mm	15 mm
	300 µg/ml	22 mm	24 mm
Control	-	0.7 mm	0.7 mm
Amoxicillin (+ Control)	**25 µg/ml**	30 mm	30 mm

The obtained results showed that Zn/Co-BC is a strong antibacterial agent toward *Klebsiellia pneumonia* **(Fig. 14, a)** and *Staphyllococus aureus* **(Fig. 14, b)**. The zone of inhibition was found to increase with increase in concentration of the nanocomposites against both bacterial species **[78]**. But the increment was slight less for *Staphyllococus aureus*, indicating better efficiency of Zn/Co-BC for Gram –ve bacteria. The values of zone of inhibition are given in **(Table 4)** by varying the concentrations of Zn/Co-BC.

Conclusion:

Current research present successfully fabrication of novel biochar (WBC) using the walnut shell and corresponding metal encapsulated nanocomposite (Zn/Co-BC) by taking appropriate proportions of salts containing Zn, Co and obtained biochar. Different analytical methods such as FTIR, FESEM, XRD, HRTEM, BET, DSC and TGA prove the synthesis of desired nanocomposite. The biochar and nanocomposite were applied and compared to remove added pollutant (ciprofloxacin) from the contaminated water and the adsorption capacity was tremendous. Furthermore, both WBC and Zn/Co-BC also investigated for excellent antibacterial activity.

References:

1. Singh, J., Verma, M., 2024, Waste derived modified biochar as promising functional material for enhanced water remediation potential, *Environ. Res.*, 245, 117999.
2. Fu, D., Kurniawan, T.A., Wang, Y., Zhou, Z., Wei, Q., Hu, Y., Othman, M.H., Chew, K.W., Goh, H.H., Gui, H., 2023, Applicability of magnetic biochar derived from Fe-enriched sewage sludge for chromate removal from aqueous solution, *Chem. Eng. Sci.*, 281, 119145.
3. Du, Z., Zheng, T., Wang, P., Hao, L., Wang, Y., 2016, Fast microwave-assisted preparation of a low-cost and recyclable carboxyl modified lignocellulose-biomass jute fiber for enhanced heavy metal removal from water, *Bioresour. Technol.*, 201, 41-49.
4. Karunaratne, T.N., Nayanathara, R.O., Navarathna, C.M., Rodrigo, P.M., Thirumalai, R.V., Pittman Jr, C.U., Kim, Y., Mlsna, T., Zhang, J., Zhang, X., 2022, Pyrolytic synthesis of graphene-encapsulated zero-valent iron nanoparticles supported on biochar for heavy metal removal, *Biochar*, 4(1), 70.
5. Qu, J., Li, Z., Wu, Z., Bi, F., Wei, S., Dong, M., Hu, Q., Wang, Y., Yu, H., Zhang, Y., 2023, Cyclodextrin-functionalized magnetic alginate microspheres for synchronous removal of lead and bisphenol a from contaminated soil, *Chem. Eng. J.*, 461, 142079.
6. Illankoon, W.A., Milanese, C., Collivignarelli, M.C., Sorlini, S., 2023, Value chain analysis of rice industry by products in a circular economy context: A review, *Waste*, 1(2), 333-369.
7. Collivignarelli, M.C., Sorlini, S., Milanese, C., Illankoon, W.A., Caccamo, F.M., Calatroni, S., 2022, Rice industry by-products as adsorbent materials for removing fluoride and arsenic from drinking water—a review, *Appl. Sci.*, 12(6), 3166.
8. Illankoon, W.A., Milanese, C., Karunarathna, A.K., Alahakoon, A.M., Rathnasiri, P.G., Medina-Llamas, M., Collivignarelli, M.C., Sorlini, S., 2023, Development of a dual-chamber pyrolizer for biochar production from agricultural waste in Sri Lanka, *Energies*, 16(4), 1819.
9. Illankoon, W.A., Sorlini, S., 2021, Technical, Economical, and Environmental Comparison of Composting and Anaerobic Digestion of Organic Waste Fraction of Municipal Solid Waste in Sri Lanka, *Proc. Waste-to-Resour.*
10. Collivignarelli, M.C., Caccamo, F.M., Bellazzi, S., Llamas, M.M., Sorlini, S., Milanese, C., 2023, Survey on Lombardy Region wastewater effluents and application of biochar from biological sewage sludge for wastewater treatment, *Water*, 15(20), 3636.
11. Munir, N., Hanif, M., Abideen, Z., Seerat, A., Hamid, M., El-Sheikh, M.A., Radicetti, E., Mancinelli, R., El-Keblawy, A., 2024, Dry fruit shell-derived biochar increases biosorption potential and detoxification of organic pollutants for land safety, *Land Degrad. Dev.*, 35(4), 1477-1494.

12. Liu, S.J., Liu, Y.G., Tan, X.F., Liu, S.B., Li, M.F., Liu, N., Yin, Z.H., Tian, S.R., Zhou, Y.H., 2019, Facile synthesis of MnOx-loaded biochar for the removal of doxycycline hydrochloride: Effects of ambient conditions and co-existing heavy metals, *J. Chem. Technol. Biotechnol.*, 94(7), 2187-2197.
13. Zhou, L., Liu, Y., Liu, S., Yin, Y., Zeng, G., Tan, X., Hu, X., Hu, X., Jiang, L., Ding, Y., Liu, S., 2016, Investigation of the adsorption-reduction mechanisms of hexavalent chromium by ramie biochars of different pyrolytic temperatures, *Bioresour. Technol.*, 218, 351-359.
14. Obey, G., Adelaide, M., Ramaraj, R., 2022, Biochar derived from non-customized matamba fruit shell as an adsorbent for wastewater treatment, *J. Bioresour. Bieprod.*, 7(2), 109-115.
15. Açıkkapı, A.N., Bani Hani, Y., Şahin Kol, H., Akalın, M.K., 2025, Production of Biochar via Pyrolysis of Apricot Seed Pulp with Calcium and Sodium Lignosulfonate, *Processes*, 13(12), 4053.
16. Guo, P., Gu, X., Li, Z., Xu, X., Cao, Y., Yang, G., Kuang, C., Li, X., Qing, Y., Wu, Y., 2025, A novel almond shell biochar modified with FeS and chitosan as adsorbents for mitigation of heavy metals from water and soil, *Sep. Purif. Technol.*, 360, 130943.
17. Raj, L., Sur, D., Rekha, M.M., Kundlas, M., Krithiga, T., Panigrahi, R., Alqhtani, H.A., Abo-Eleneen, R.E., Sankhla, M.S., Verma, M., 2025, Biochar derived from pistachio shells: A novel adsorbent for efficient lead sequestration in water treatment, *J. Mol. Struct.*, 1344, 142930.
18. Liao, Z., Li, P., Cai, X., Sun, Z., Feng, H., Huang, Z., Wei, Y., Yin, Q., Liu, G., Li, C., Shi, Y., 2026, Long-term peanut shell biochar application improves soil fertility and bacterial network stability across tobacco-growing regions in China, *Biochar*, 8(1), 63.
19. Ñanculeo, J., Andreu, T., Sirés, I., Ramírez, A., Cea, M., Nahuelcura, B., Valenzuela, G., Garrido-Miranda, K., González, M.E., 2025, Development of hazelnut shell-derived biochar to support a bifunctional MoCo electrocatalyst for HER/OER in alkaline medium, *Biochar*, 7(1), 72.
20. Min, K.H., Kim, K.H., Seo, J.H., Pack, S.P., 2025, Biochar utilization in antimicrobial, anticancer, and biosensing applications: a review, *Biomolecules*, 15(6), 760.
21. Zhi, K., Zhang, J., Zhang, J., Liu, Z., Cui, H., Zhang, J., Wang, Y., Feng, J., Mei, Y., Liu, Z., 2026, Application of Biochar-Based Materials as Adsorbents for Aquatic Environment Remediation: Preparation, Mechanisms, and Performance Evaluation, *J. Hazard. Mater. Adv.*, 101321.
22. Thabede, P.M., Shooto, N.D., 2025, The removal of methyl orange from water using biochar derived from a blend of carrot and potato peels, *Desalination Water Treat.*, 101584.
23. Mudhoo, A., 2025, Unveiling new insights: Revised Temkin adsorption isotherm parameters from fresh curve fits in adsorption studies, *Chem. Eng. Sci.*, 311, 121585.
24. Magdy, A., Mostafa, M.R., Moustafa, S.A., Mohamed, G.G., Fouad, O.A., 2024, Kinetics and adsorption isotherms studies for the effective removal of Evans blue dye from an aqueous solution utilizing forsterite nanoparticles, *Sci. Rep.*, 14(1), 24392.
25. Musah, M., Azeh, Y., Mathew, J.T., Umar, M.T., Abdulhamid, Z., Muhammad, A.I., 2022, Adsorption kinetics and isotherm models: a review, *CaJoST*, 4(1), 20-26.
26. Al-Muttair, A.K., Al Easawi, N.A., Mustafa, S.A., 2022, Using adsorption as means to treat water pollution, *J. Biotechnol. Res. Cent.*, 16(1), 37-47.
27. Mukherjee, D., Sil, M., Goswami, A., Bhattacharya, D., Nag, M., Lahiri, D., Sharma, K., Verma, R., 2025, Synthesis, modification and antimicrobial potential of biochar and its modifications against water-borne pathogens: A review, *Results Surf. Interfaces*, 18, 100438.

28. Alfattani, R., Shah, M.A., Siddiqui, M.I., Ali, M.A., Alnaser, I.A., 2021, Bio-char characterization produced from walnut shell biomass through slow pyrolysis: sustainable for soil amendment and an alternate bio-fuel, *Energies*, 15(1), 1.
29. Handiso, B., Pääkkönen, T., Wilson, B.P., 2024, Effect of pyrolysis temperature on the physical and chemical characteristics of pine wood biochar, *Waste Manage. Bull.*, 2(4), 281-287.
30. Adeniyi, A.G., Ighalo, J.O., Onifade, D.V., 2021, Production of biochar from elephant grass (Pernisetum purpureum) using an updraft biomass gasifier with retort heating, *Biofuels*, 12(10), 1269-1276.
31. Arundina, R.Y., Togatorop, E.R., Sutan, S.M., Marlina, R., 2024, Structural properties and adsorption capability of activated carbon from oil palm shell by using hydrothermal-pyrolysis method, *AIP Conf. Proc.*, 2973(1), 060014.
32. Xie, Z., Guan, W., Ji, F., Song, Z., Zhao, Y., 2014, Production of biologically activated carbon from orange peel and landfill leachate subsequent treatment technology, *J. Chem.*, 2014, 491912.
33. Xie, Z., Guan, W., Ji, F., Song, Z., Zhao, Y., 2014, Production of biologically activated carbon from orange peel and landfill leachate subsequent treatment technology, *J. Chem.*, 2014, 491912.
34. Aldabagh, I.S., Hummadi, K.K., 2024, Effectiveness and analysis of synthesis nanoparticles walnut shells/zinc oxide to reduce trimethoprim from aqueous solutions, *Case Stud. Chem. Environ. Eng.*, 9, 100674.
35. Kritikaki, A., Karmali, V., Vathi, D., Bartzas, G., Komnitsas, K., 2025, Advanced characterization of biochars produced from three different organic-based feedstocks and their potential applications, *Circ. Econ. Sustain.*, 5(8), 7465-7488.
36. Khan, N.I., Halder, S., Goyat, M.S., Borah, L.N., Das, S., 2023, Repetitive self-healing of Diels–Alder grafted graphene nanoplatelet reinforced carbon fiber reinforced polymer composites with outstanding mechanical properties, *Soft Matter*, 19(17), 3121-3135.
37. Niu, H., Jin, H., Sun, Q., Shi, Y., Zhang, X., Cai, Y., 2021, Activation of biochars by waste phosphoric acids: an integrated disposal route of waste acids and solid waste, *ACS Sustainable Chem. Eng.*, 9(48), 16403-16414.
38. Siddiqui, A.J., Kumari, N., Adnan, M., Kumar, S., Abdelgadir, A., Saxena, J., Badraoui, R., Snoussi, M., Khare, P., Singh, R., 2023, Impregnation of modified magnetic nanoparticles on low-cost agro-waste-derived biochar for enhanced removal of pharmaceutically active compounds: performance evaluation and optimization using response surface methodology, *Water*, 15(9), 1688.
39. El-Shafie, A.S., Barah, F.G., Abouseada, M., El-Azazy, M., 2023, Performance of pristine versus magnetized orange peels biochar adapted to adsorptive removal of daunorubicin: eco-structuring, kinetics and equilibrium studies, *Nanomaterials*, 13(9), 1444.
40. Hinsene, H., Sukpirom, N., Bhawawet, N., Imyim, A., 2026, Deep eutectic solvent-modified magnetic biochar from sugarcane bagasse for enhanced removal of toxic metals and pharmaceuticals, *Sep. Purif. Technol.*, 384, 137339.
41. Yu, J., Chen, X., Huang, L., Chen, H., Tao, H., 2026, Unraveling the “Black Box”: Challenges and Perspectives in Elucidating Catalytic Mechanisms of Metal–Biomass Carbon Hybrids for Persulfate Activation, *Water*, 18(7), 838.
42. Chen, Y., Yang, Y., Ren, N., Duan, X., 2023, Single-atom catalysts derived from biomass: low-cost and high-performance persulfate activators for water decontamination, *Curr. Opin. Chem. Eng.*, 41, 100942.

43. Dong, Z., Wu, X., Yu, T., Li, C., Zhang, H., Wang, J., Rezayan, A., Wang, A., 2026, Enhanced Adsorption Performance of Zn/Co-Modified Biochar for Cu (II) and Cd (II), *ACS Omega*, 11(16), 24509.
44. Mehrasa, S., Saboor, F.H., Asgari, M., 2024, Biochar Modification for Removal of Inorganic and Organic Contaminants from Industrial Effluent, *ACS Symp. Ser.*, 1475, 131-156.
45. Hong, Y., Zhou, X., Zeng, F., 2025, Integrating carbon-coated Cu/Cu2O nanoparticles with biochars enabled efficient capture and electrocatalytic reduction of CO2, *Catalysts*, 15(8), 767.
46. Chen, C., Zhang, J., Qi, Y., Zhang, J., Guo, T., Wang, H., 2024, Locust leaves-derived biochar coupled CuxO composites for efficient electrocatalytic CO2 reduction, *Fuel*, 372, 132245.
47. Tang, H., Zhou, Y., Liu, Y., Qian, Y., Qiu, Z., Chen, A., Lin, B.L., 2023, Rationally designed hierarchical carbon supported CuO nano-sheets for highly efficient electroreduction of CO2 to multi-carbon products, *J. CO2 Util.*, 67, 102320.
48. Ullah, M.H., Rahman, M.J., 2025, Efficient Cr (VI) removal from tannery wastewater using Co-Zn ferrite-modified water hyacinth biochar: mechanisms and optimization, *Environ. Monit. Assess.*, 197(6), 623.
49. Wang, S., Zhao, H., Liu, J., Wang, X., Li, J., Shi, E., Wang, C., Yang, J., Zhang, Z., 2023, A study on and adsorption mechanism of ammonium nitrogen by modified corn straw biochar, *R. Soc. Open Sci.*, 10(2), 221535.
50. Darabdhara, J., Ahmaruzzaman, M., 2022, Recent developments in MOF and MOF based composite as potential adsorbents for removal of aqueous environmental contaminants, *Chemosphere*, 304, 135261.
51. Wang, J., Tan, Y., Yang, H., Zhan, L., Sun, G., Luo, L., 2023, On the adsorption characteristics and mechanism of methylene blue by ball mill modified biochar, *Sci. Rep.*, 13(1), 21174.
52. Banerjee, S., Chattopadhyaya, M.C., 2017, Adsorption characteristics for the removal of a toxic dye, tartrazine from aqueous solutions by a low cost agricultural by-product, *Arab. J. Chem.*, 10, S1629-S1638.
53. Marzbali, M.H., Mir, A.A., Pazoki, M., Pourjamshidian, R., Tabeshnia, M., 2017, Removal of direct yellow 12 from aqueous solution by adsorption onto spirulina algae as a high-efficiency adsorbent, *J. Environ. Chem. Eng.*, 5(2), 1946-1956.
54. Andrade, C.A., Zambrano-Intriago, L.A., Oliveira, N.S., Vieira, J.S., Quiroz-Fernández, L.S., Rodríguez-Díaz, J.M., 2020, Adsorption behavior and mechanism of oxytetracycline on rice husk ash: kinetics, equilibrium, and thermodynamics of the process, *Water Air Soil Pollut.*, 231(3), 103.
55. Lin, D., Wu, F., Hu, Y., Zhang, T., Liu, C., Hu, Q., Hu, Y., Xue, Z., Han, H., Ko, T.H., 2020, Adsorption of dye by waste black tea powder: parameters, kinetic, equilibrium, and thermodynamic studies, *J. Chem.*, 2020, 5431046.
56. Singh, S., Prajapati, A.K., Chakraborty, J.P., Mondal, M.K., 2023, Adsorption potential of biochar obtained from pyrolysis of raw and torrefied Acacia nilotica towards removal of methylene blue dye from synthetic wastewater, *Biomass Convers. Biorefin.*, 13(7), 6083-6104.
57. El Maguana, Y., Elhadiri, N., Benchanaa, M., Chikri, R., 2020, Activated carbon for dyes removal: modeling and understanding the adsorption process, *J. Chem.*, 2020, 2096834.
58. Wang, J., Tan, Y., Yang, H., Zhan, L., Sun, G., Luo, L., 2023, On the adsorption characteristics and mechanism of methylene blue by ball mill modified biochar, *Sci. Rep.*, 13(1), 21174.

59. Hameed, B.H., Mahmoud, D.K., Ahmad, A.L., 2008, Equilibrium modeling and kinetic studies on the adsorption of basic dye by a low-cost adsorbent: Coconut (Cocos nucifera) bunch waste, *J. Hazard. Mater.*, 158(1), 65-72.
60. Ambaye, T.G., Vaccari, M., van Hullebusch, E.D., Amrane, A., Rtimi, S.J., 2021, Mechanisms and adsorption capacities of biochar for the removal of organic and inorganic pollutants from industrial wastewater, *Int. J. Environ. Sci. Technol.*, 18(10), 3273-3294.
61. Liu, Z., Zhang, F.S., 2009, Removal of lead from water using biochars prepared from hydrothermal liquefaction of biomass, *J. Hazard. Mater.*, 167(1-3), 933-939.
62. Liu, Q.Y., Yang, F., Sun, X.F., Liu, Z.H., Li, G., 2017, Preparation of biochar catalyst with saccharide and lignocellulose residues of corncob degradation for corncob hydrolysis into furfural, *J. Mater. Cycles Waste Manag.*, 19(1), 134-143.
63. Lu, K., Yang, X., Gielen, G., Bolan, N., Ok, Y.S., Niazi, N.K., Xu, S., Yuan, G., Chen, X., Zhang, X., Liu, D., 2017, Effect of bamboo and rice straw biochars on the mobility and redistribution of heavy metals (Cd, Cu, Pb and Zn) in contaminated soil, *J. Environ. Manage.*, 186, 285-292.
64. Islam, I.U., Ahmad, M., Ahmad, M., Rukh, S., Ullah, I., 2022, Kinetic studies and adsorptive removal of chromium Cr (VI) from contaminated water using green adsorbent prepared from agricultural waste, rice straw, *Eur. J. Chem.*, 13, 78-90.
65. Hu, X., Ding, Z., Zimmerman, A.R., Wang, S., Gao, B., 2015, Batch and column sorption of arsenic onto iron-impregnated biochar synthesized through hydrolysis, *Water Res.*, 68, 206-216.
66. Hikmat, K., Aziz, H., Fatah, N.M., 2024, Advancements in Application of Modified Biochar as a Green and Low-cost Adsorbent for Wastewater Remediation From Organic Dyes, *Int. J. Chem. Eng.*, 2024, 6505349.
67. Goswami, L., Kushwaha, A., Kafle, S.R., Kim, B.S., 2022, Surface modification of biochar for dye removal from wastewater, *Catalysts*, 12(8), 817.
68. Trivedi, Y., Sharma, M., Mishra, R.K., Sharma, A., Joshi, J., Gupta, A.B., Achintya, B., Shah, K., Vuppaladadiyam, A.K., 2025, Biochar potential for pollutant removal during wastewater treatment: A comprehensive review of separation mechanisms, technological integration, and process analysis, *Desalination*, 596, 118509.
69. Verma, N., Devi, N.L., 2025, Removal of atmospheric pollutants using biochar: preparation, application, regeneration and its future research, *Air Quality, Atmos. Health*, 18(4), 1205-1224.
70. Gwenzi, W., Chaukura, N., Wenga, T., Mtisi, M., 2021, Biochars as media for air pollution control systems: Contaminant removal, applications and future research directions, *Sci. Total Environ.*, 753, 142249.
71. Zhang, N., Reguyal, F., Praneeth, S., Sarmah, A.K., 2023, A novel green synthesized magnetic biochar from white tea residue for the removal of Pb (II) and Cd (II) from aqueous solution: Regeneration and sorption mechanism, *Environ. Pollut.*, 330, 121806.
72. Bambal, A., Jugade, R., Khapre, M., Saravanan, D., 2025, Carbonization of golden shower pods to high surface area biochar for decontamination of cationic dyes and regeneration study by gamma radiations, *Next Sustain.*, 5, 100064.
73. Baaloudj, O., Chiron, S., Zizzamia, A.R., Trotta, V., Del Buono, D., Puglia, D., Rallini, M., Brienza, M., 2025, Efficient biochar regeneration for a circular economy: Removing emerging contaminants for sustainable water treatment, *Colloids Surf. A Physicochem. Eng. Asp.*, 705, 135730.

74. Amusat, S.O., Kebede, T.G., Nxumalo, E.N., Dube, S., Nindi, M.M., 2023, Green synthesis of surface modified biochar for simultaneous removal of steroidal hormones and heavy metals from wastewater: optimisation by central composite design, *Water*, 15(20), 3703.
75. Alsawy, T., Rashad, E., El-Qelish, M., Mohammed, R.H., 2022, A comprehensive review on the chemical regeneration of biochar adsorbent for sustainable wastewater treatment, *NPJ Clean Water*, 5(1), 29.
76. Tran, N.D., Bui, T.H., Nguyen, A.P., Nguyen, T.T., Nguyen, V.M., Duong, N.L., Nguyen, T., 2022, The ability of silver-biochar green-synthesized from Citrus maxima peel to adsorb pollutant organic compounds and antibacterial activity, *Green Chem. Lett. Rev.*, 15(1), 18-27.
77. Moreno, E., Gualle, A., Vizuete, K., Debut, A., Orejuela, L., Ponce, S., 2024, Engineered biochar: novel silver loading onto biochar using agri-waste extract assisted by led light for catalyst and antibacterial capabilities, *Waste Biomass Valorization*, 15(12), 6577-6586.
78. Allah, M.A., Ibrahim, H.K., Alshamsi, H.A., 2025, Enhanced adsorption, anticancer and antibacterial potentials of Pontederia crassipes L. extract mediated ecofriendly synthesized ZnO/biochar nanohybrid, *Inorg. Chem. Commun.*, 171, 113538.

ACKNOWLEDGEMENTS:
The authors would like to thank Punjab University (PU), India, and the Indian Institute of Technology (IIT), Mandi, India, for providing the instrumental facilities required to conduct this research.